Electronic Supplementary Information

Electronic Structure and Magnetic Properties of Rhenium Complexes with Iminoxolene Ligand: Experimental and Computational Studies

Pavel A. Petrov,[†]* Alexey A. Dmitriev,[‡]* Anastasiia D. Semikina,[†] Ilia V. Eltsov,[‖] Taisiya S. Sukhikh,[†] Alexander N. Lavrov,[†] Artem L. Gushchin,[†] Maxim N. Sokolov,[†] and Nina P. Gritsan[‡]

[†] Nikolaev Institute of Inorganic Chemistry SB RAS, Prosp. Lavrentieva 3, 630090 Novosibirsk, Russia;
[‡] Voevodsky Institute of Chemical Kinetics and Combustion SB RAS, Institutskaya 3, 630090 Novosibirsk, Russia;
[‖] Novosibirsk State University, Pirogova 2, 630090 Novosibirsk, Russia.

I. Crystal structures

Table S1. Crystal data and structure refinement for structures 1, 2, 2·4C_6H_6, and 3·0.5C_4H_8O.

	1	**2**	**2**·4C_6H_6	**3**·0.5C_4H_8O
Empirical formula	$C_{44}H_{52}Cl_3NOPRe$	$C_{44}H_{52}Cl_3NO_2PRe$	$C_{68}H_{76}Cl_3NO_2PRe$	$C_{38}H_{51}Cl_4CoNO_{1.5}Re$
Formula weight	934.38	950.38	1262.81	932.72
Temperature/K	150(2)	150(2)	150(2)	150(2)
Crystal system	triclinic	monoclinic	triclinic	monoclinic
Space group	*P*–1	$P2_1/c$	*P*–1	*C*2/*c*
a/Å	11.4320(2)	11.2614(3)	11.5787(3)	40.471(3)
b/Å	13.6478(3)	13.6220(3)	11.9253(3)	10.0512(6)
c/Å	13.7555(3)	27.5513(9)	23.4028(6)	19.8546(14)
α/°	99.2850(10)	90	79.9600(10)	90
β/°	93.4870(10)	95.8020(10)	83.9670(10)	101.752(4)
γ/°	96.5410(10)	90	79.2710(10)	90
Volume/Å^3	2097.37(7)	4204.8(2)	3117.51(14)	7907.2(9)
Z	2	4	2	8
ρ_{calc} / g cm^{-3}	1.480	1.501	1.345	1.567
μ/mm^{-1}	3.160	3.155	2.146	11.902
F(000)	944.0	1920.0	1296.0	3744.0
Crystal size/mm	0.11×0.1×0.1	0.15×0.11×0.06	0.12×0.12×0.09	0.13×0.12×0.03
2Θ range for data collection/°	4.414–61.136	3.338–57.44	4.6–57.412	4.46–140.478
Index ranges	$-16 \le h \le 16$, $-19 \le k \le 19$, $-19 \le l \le 19$	$-15 \le h \le 15$, $-18 \le k \le 18$, $-37 \le l \le 36$	$-14 \le h \le 15$, $-16 \le k \le 16$, $-31 \le l \le 31$	$-49 \le h \le 48$, $-10 \le k \le 11$, $-12 \le l \le 23$
Reflections collected	53346	21029	48882	7203
Independent reflections	12800	10878	15973	7203
R_{int}	0.0423	0.0344	0.0365	0.1077
Data/restraints/parameters	12800/0/470	10878/0/479	15973/198/815	7203/150/506
Goodness-of-fit on F^2	1.041	1.059	1.042	1.079
Final *R* indexes [$I>=2\sigma(I)$]	R_1 = 0.0257, wR_2 = 0.0495	R_1 = 0.0353, wR_2 = 0.0741	R_1 = 0.0253, wR_2 = 0.0479	R_1 = 0.0565, wR_2 = 0.1391
Final *R* indexes [all data]	R_1 = 0.0298, wR_2 = 0.0519	R_1 = 0.0496, wR_2 = 0.0778	R_1 = 0.0309, wR_2 = 0.0495	R_1 = 0.0614, wR_2 = 0.1426
Largest diff. peak/hole / e Å^{-3}	1.22/–0.67	1.28/–1.21	0.43/–0.46	2.06/–1.58
CCDC	2340971	2340969	2340970	2493258

II. NMR spectroscopy

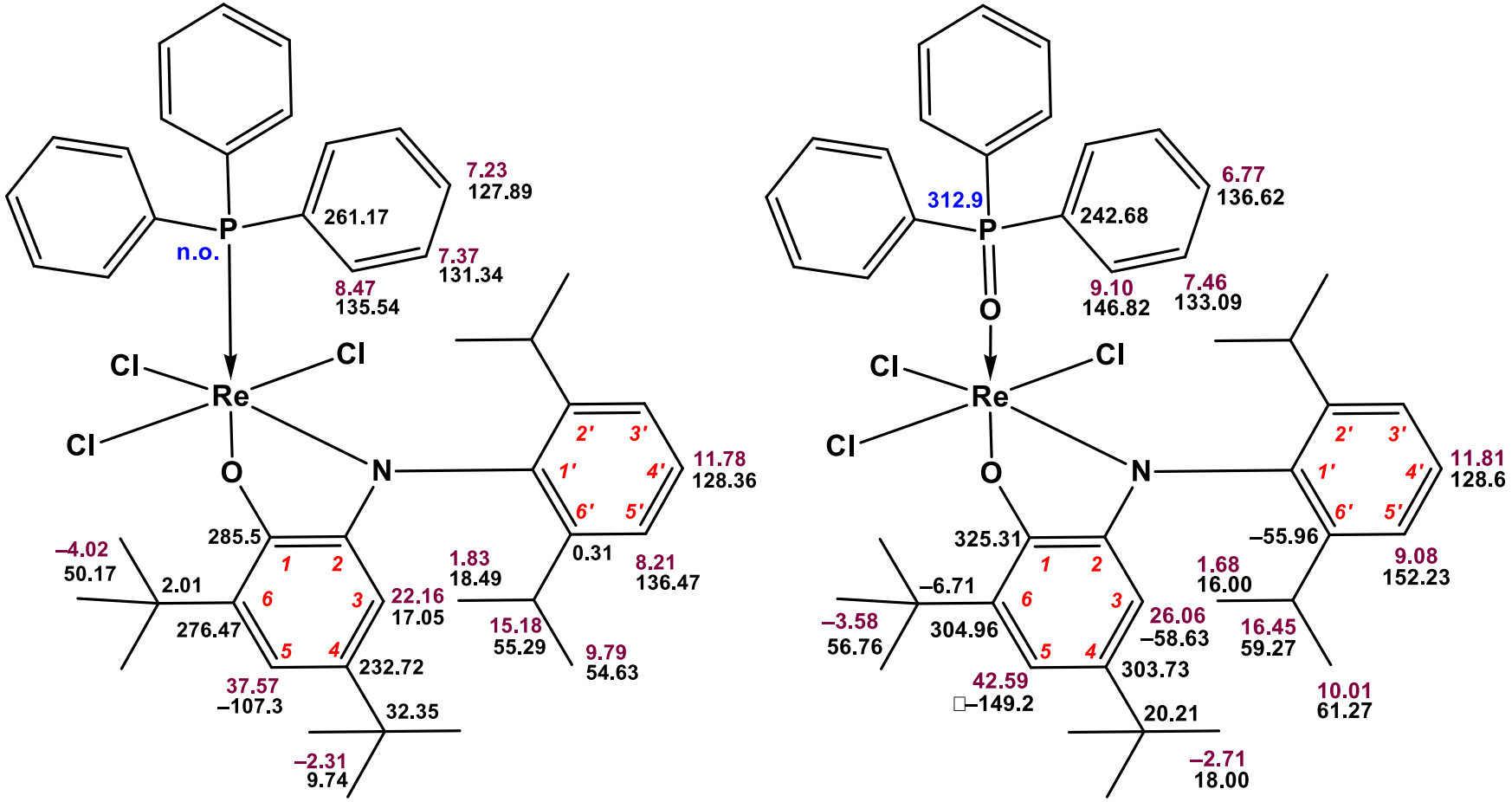

Fig. S1. Assignment scheme of ^{1}H (magenta), ^{13}C (black) and ^{31}P (blue) chemical shifts for complexes **1** (top) and **2** (bottom) (C_6D_6, ambient temperature).

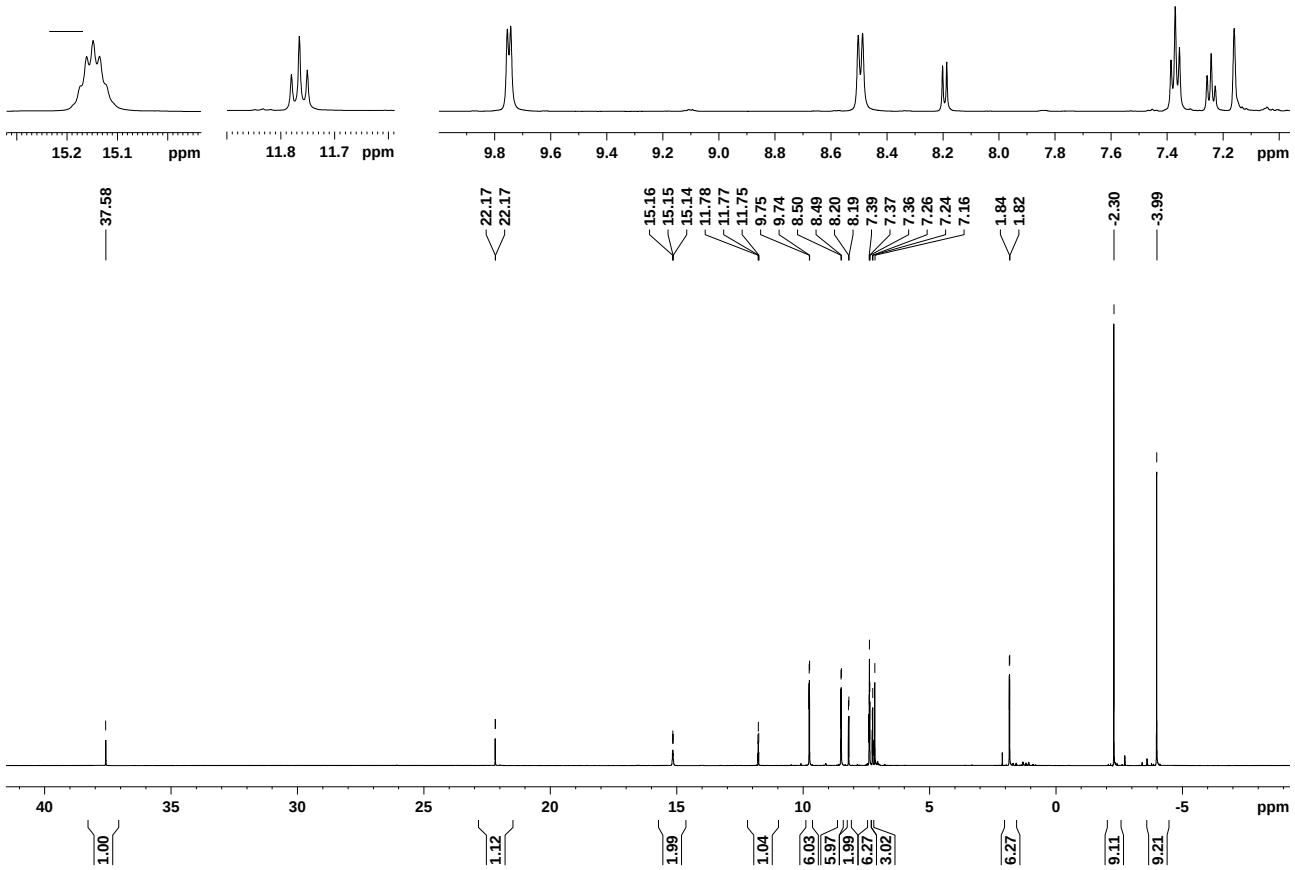

Fig. S2. ^{1}H NMR spectrum of complex **1** (C_6D_6, ambient temperature).

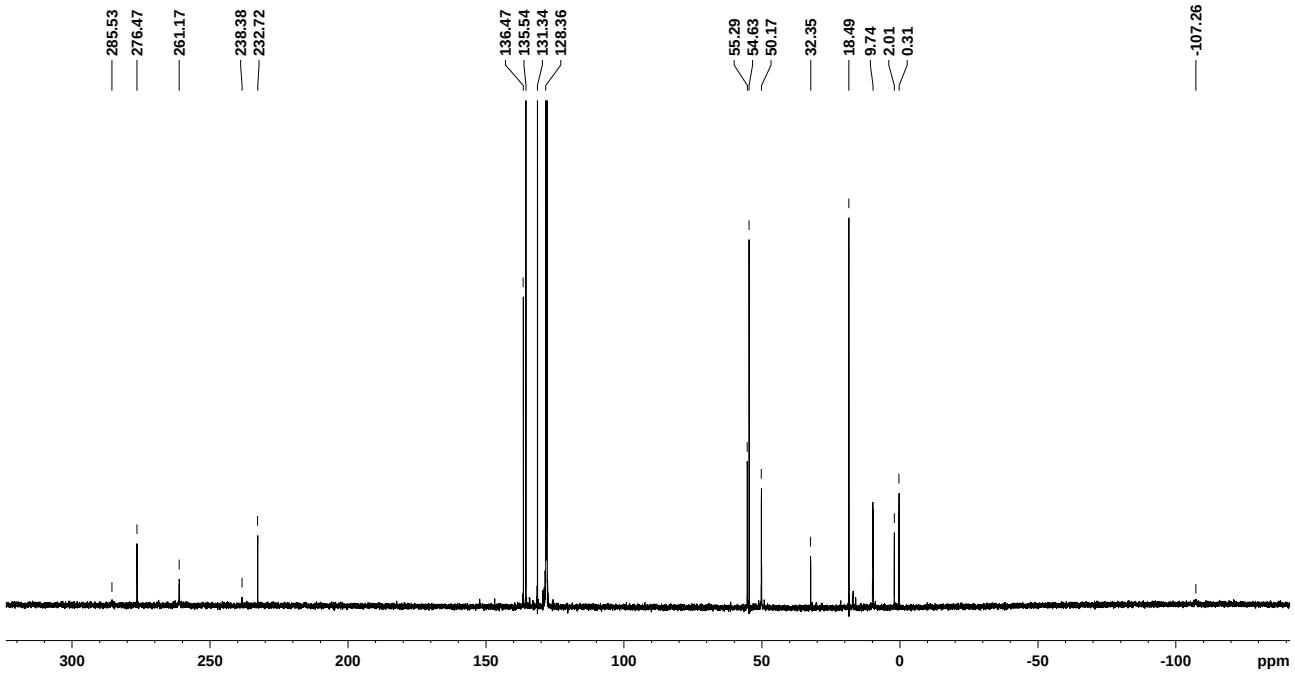

Fig. S3. ^{13}C{^{1}H} NMR spectrum of complex **1** (C_6D_6, ambient temperature).

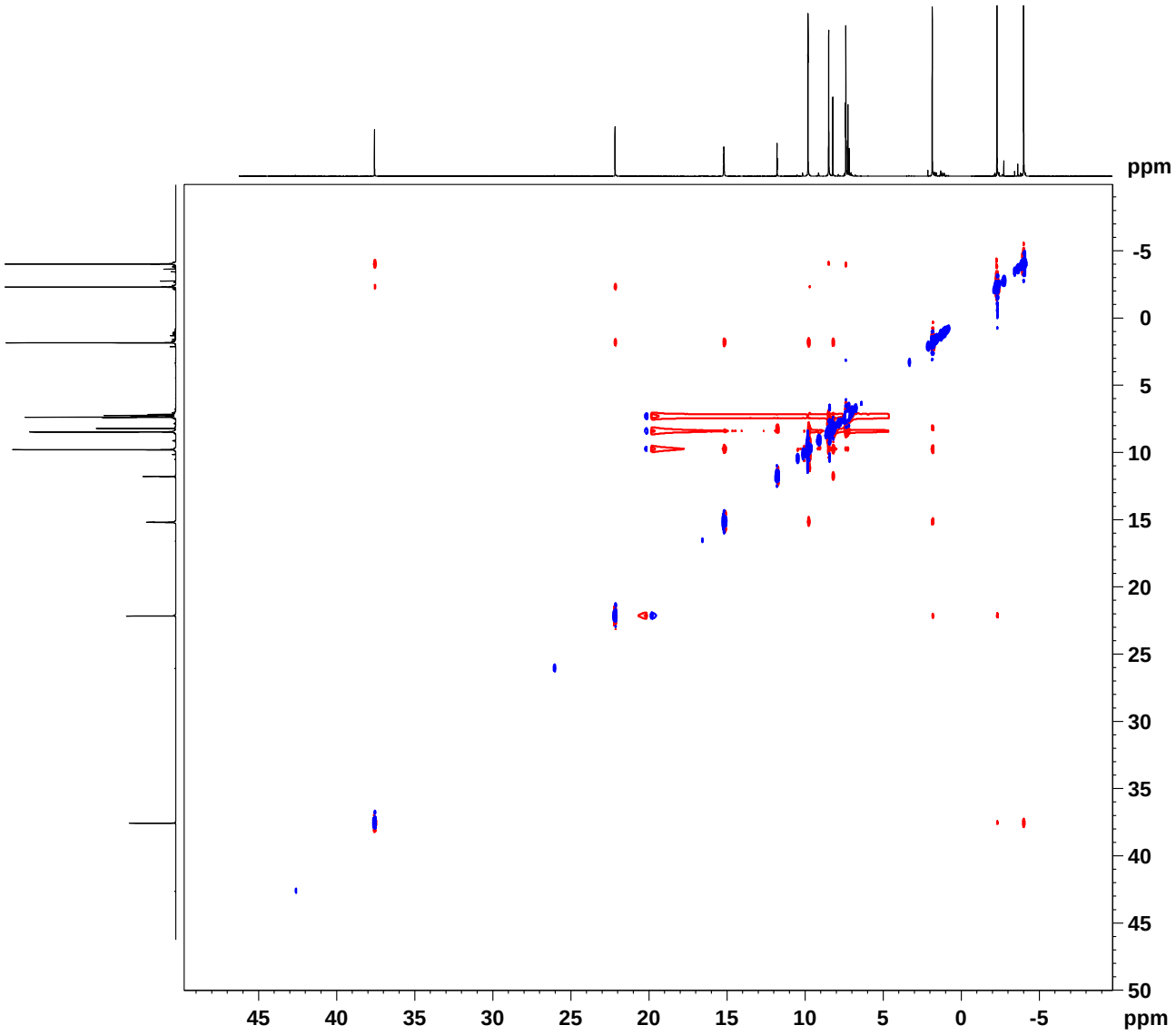

Fig. S4. $^{1}H^{1}H$ NOESY NMR spectrum of complex **1** (C_6D_6, ambient temperature).

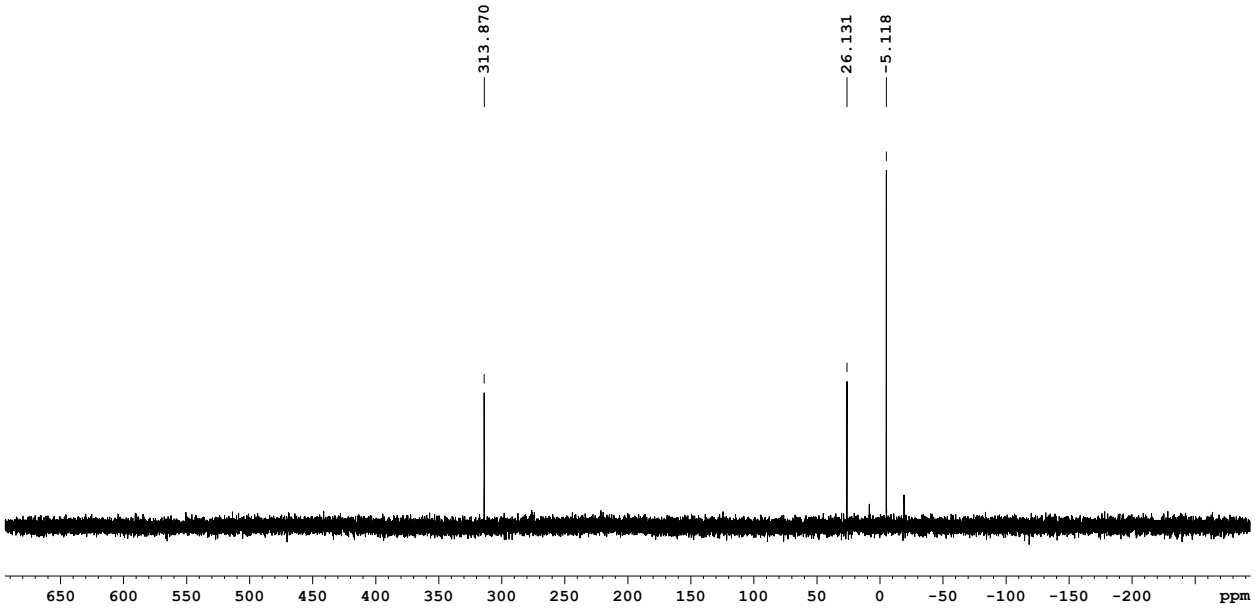

Fig. S5. ^{31}P NMR spectrum of complex **1** (C_6D_6, ambient temperature).

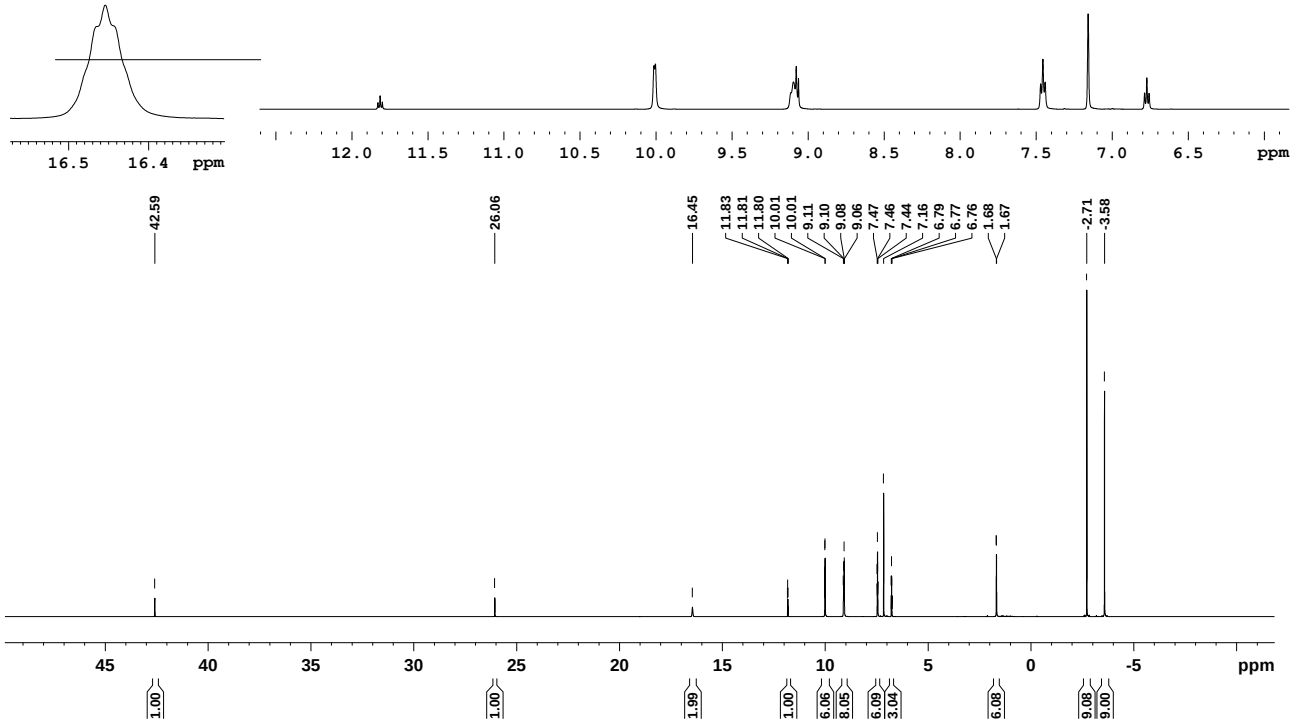

Fig. S6. ^{1}H NMR spectrum of complex **2** (C_6D_6, ambient temperature).

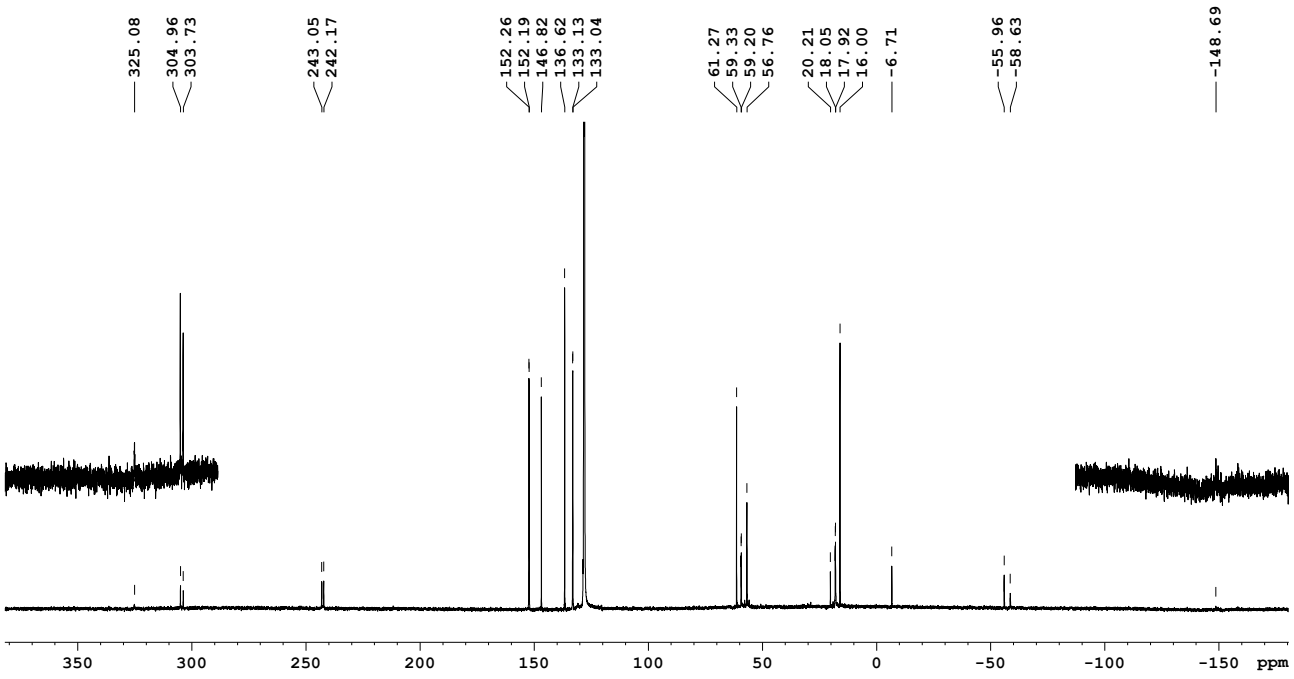

Fig. S7. $^{13}C\{^{1}H\}$ NMR spectrum of complex **2** (C_6D_6, ambient temperature).

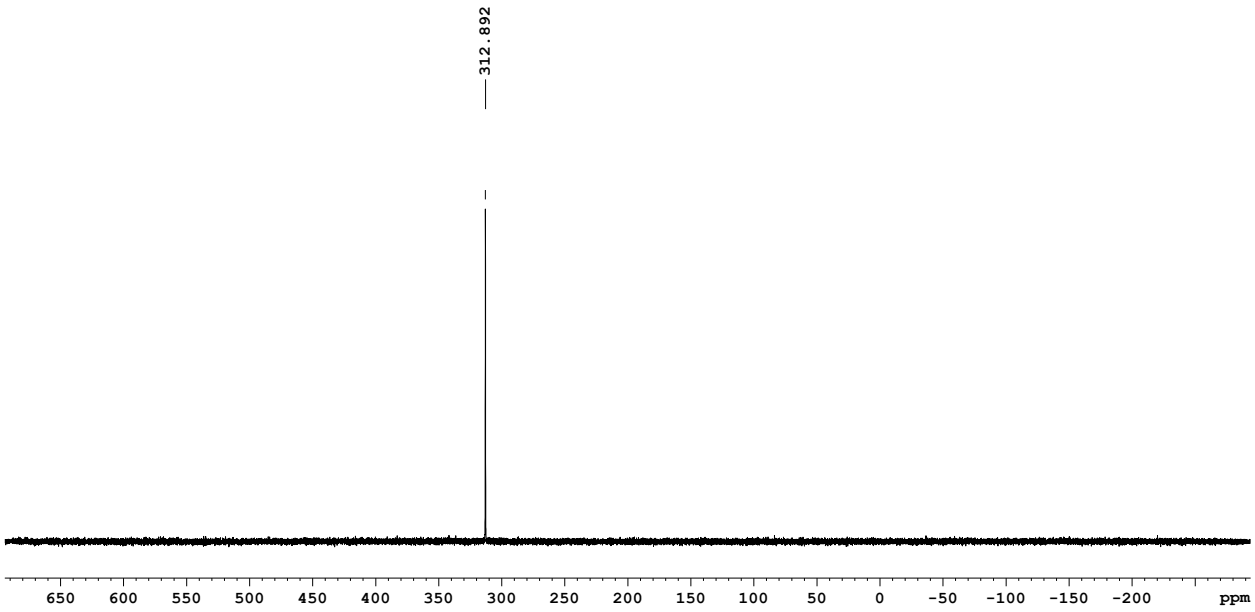

Fig. S8. ^{31}P NMR spectrum of complex **2** (C_6D_6, ambient temperature).

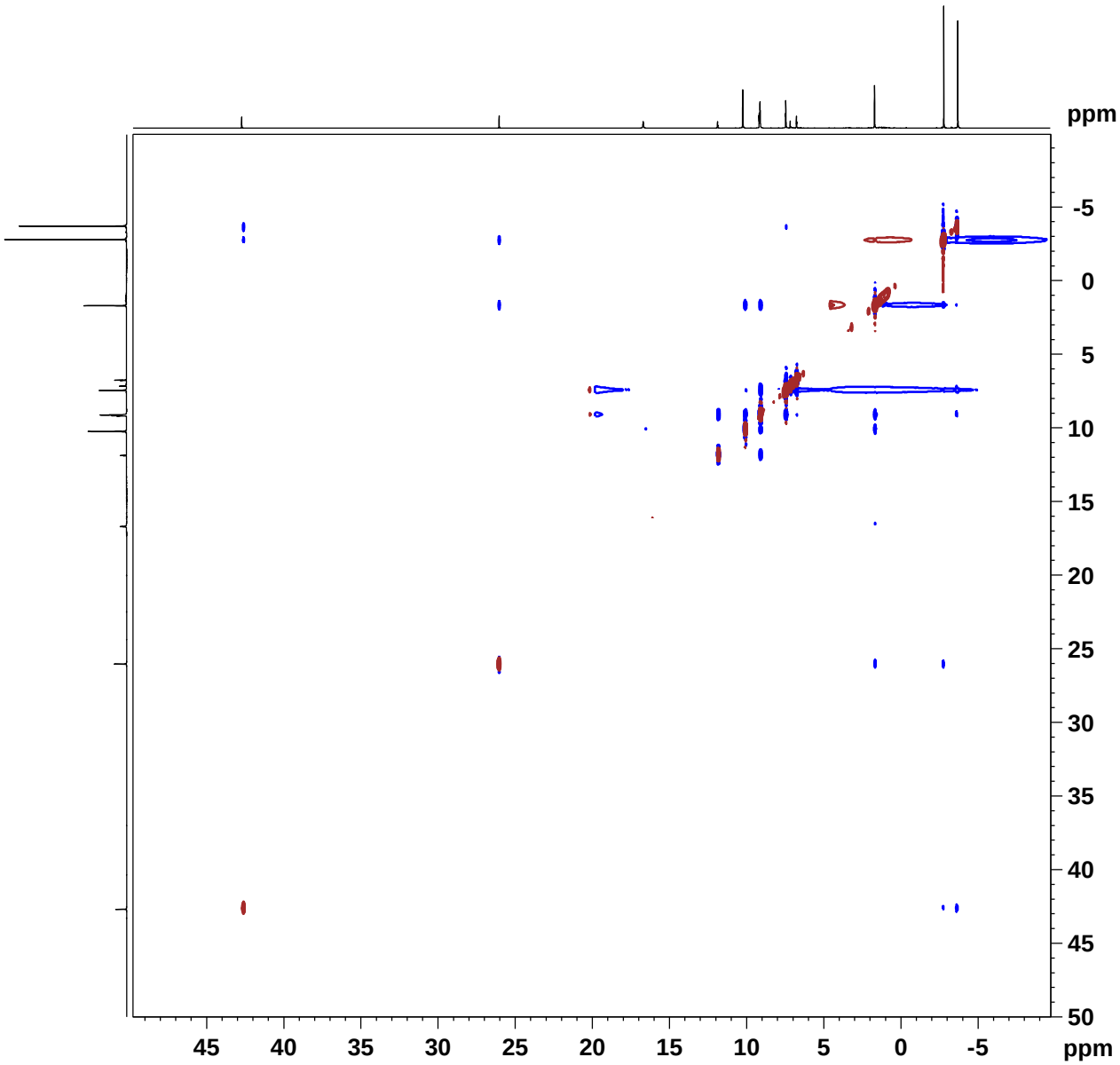

Fig. S9. $^{1}H^{1}H$ NOESY NMR spectrum of complex **2** (C_6D_6, ambient temperature).

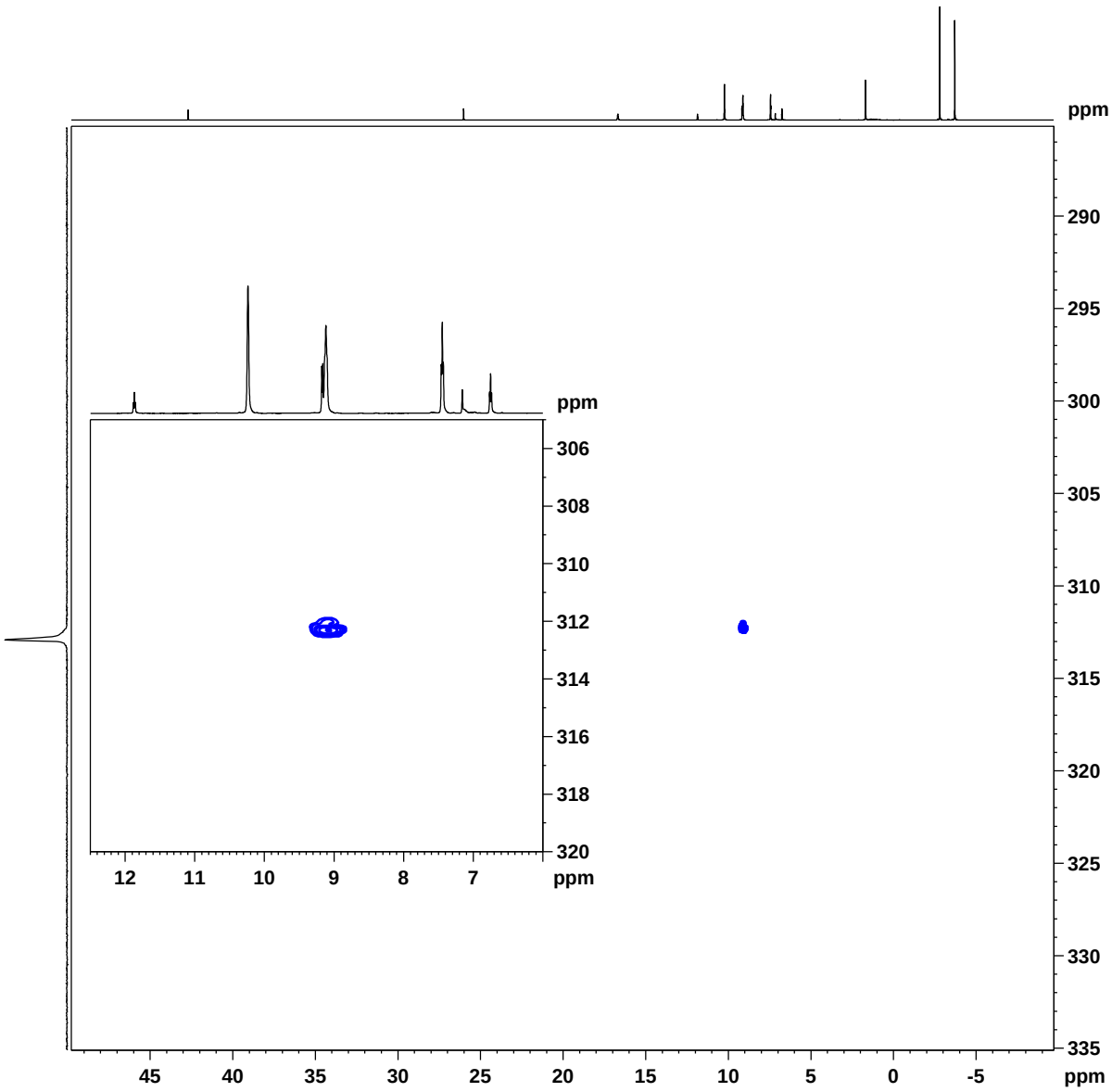

Fig. S10. $^{1}H^{31}P$ HMBC NMR spectrum of complex **2** (C_6D_6, ambient temperature).

III. Quantum Chemical Calculations

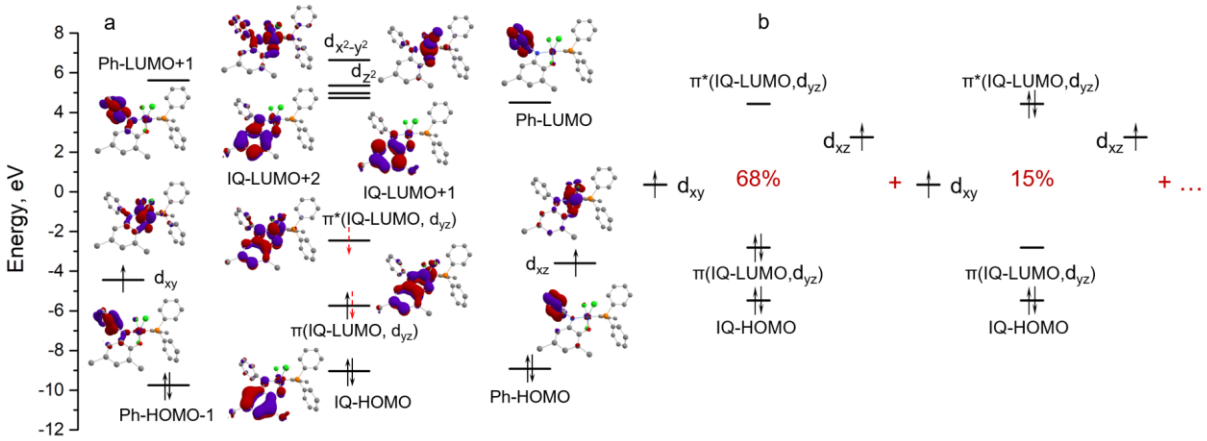

Fig. S11. a) Molecular orbitals of the active space (isosurface at 0.03) in the calculations at the DKH2-SA-CASSCF(10,13)/DKH-def2-TZVP level for complex **1m** (hydrogen atoms are omitted for clarity) with 1 quintet, 9 triplet, and 8 singlet states. The energies of active MOs were estimated by Fock operator averaging. b) The major electronic configurations contributing to the wave function of the ground triplet state of complex **1m**.

Note, that at all levels of theory, calculations predict the ground triplet state of complex **1**, well isolated from excited states. At the SA-CASSCF level, the quintet state is at 4147 cm^{-1} and the singlet state at 8796 cm^{-1}, while at the SA-CASSCF/NEVPT2 and SA-CASSCF/QD-NEVPT2 level, the singlet is at 4883 and 5054 cm^{-1} and the quintet at 7517 and 7805 cm^{-1}.

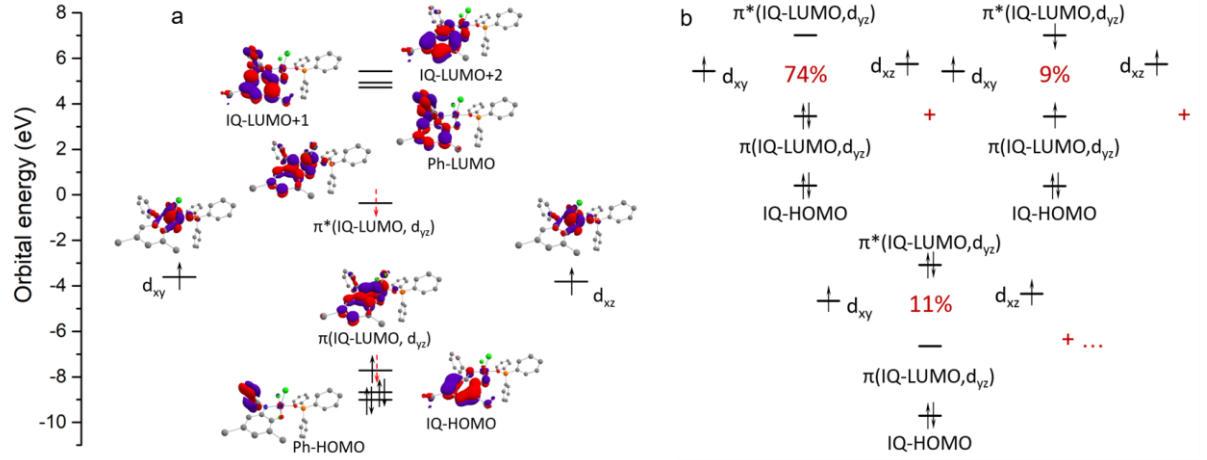

Fig. S12. Molecular orbitals of the active space (isosurface at 0.03)in calculations at the DKH2-CASSCF(10,13)/DKH-def2-TZVP level for the **2m** complex (hydrogen atoms are omitted for clarity). The energies of active MOs are estimated by Fock operator averaging. b) The major electronic configurations contributing to the wave function of the ground triplet state of complex **2m**.

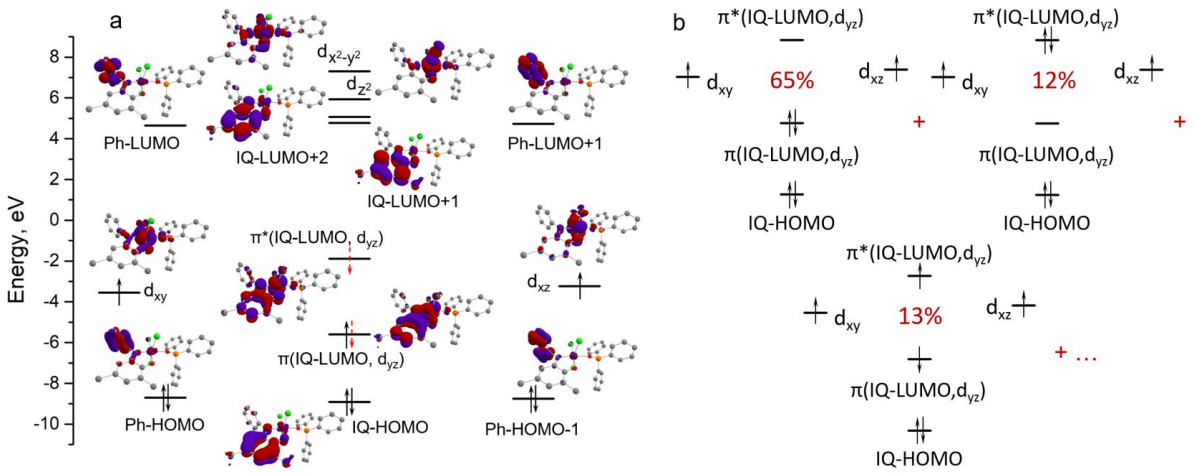

Fig. S13. Molecular orbitals of the active space (isosurface at 0.03) in calculations at the DKH2-SA-CASSCF(10,13)/DKH-def2-TZVP level for the **2m** complex (hydrogen atoms are omitted for clarity) with 1 quintet, 9 triplet, and 8 singlet states. The energies of active MOs are estimated by Fock operator averaging. b) The major electronic configurations contributing to the wave function of the ground triplet state of the **2m** complex.

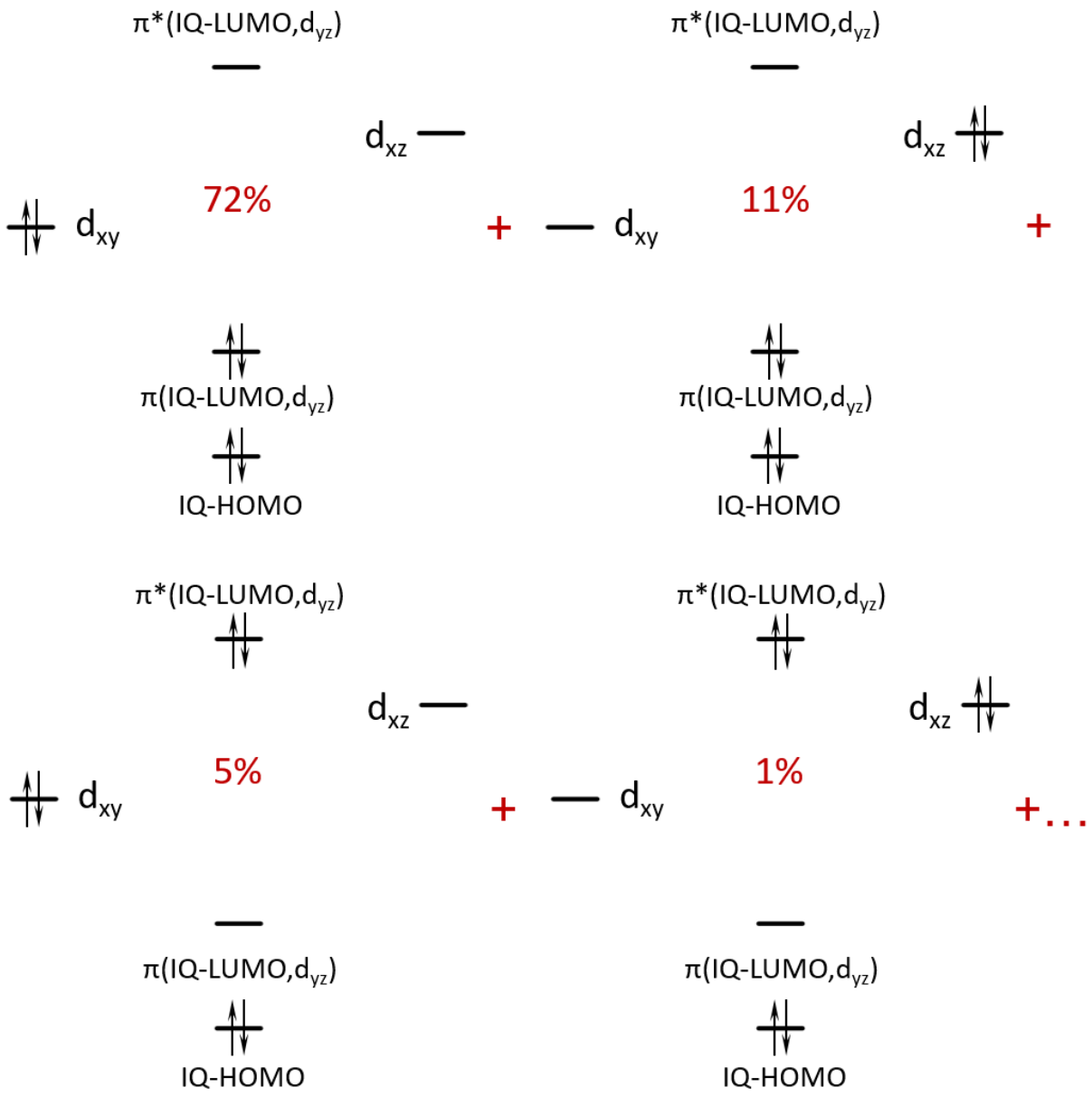

Fig. S14. Occupations of the active MOs in the configurations contributing mainly to the wave function of the lowest excited singlet state of complex **1m**.

The first excited singlet state of **1m** has, like the ground triplet state, a strongly multi-configuration wave function with major contributions from four electronic configurations with doubly occupied d_{xy} or d_{xz} orbitals and redistribution of electrons between π- and π*-orbitals (Fig. S13). The wave function of the first excited quintet state has a dominant single configuration (90 %) with singly occupied d_{xy}, d_{xz}, π- and π*-orbitals. The Mulliken spin population on Re in the quintet state is 2.73 at the CASSCF level, while the spin population of the iminooxolene ligand is 1.07.

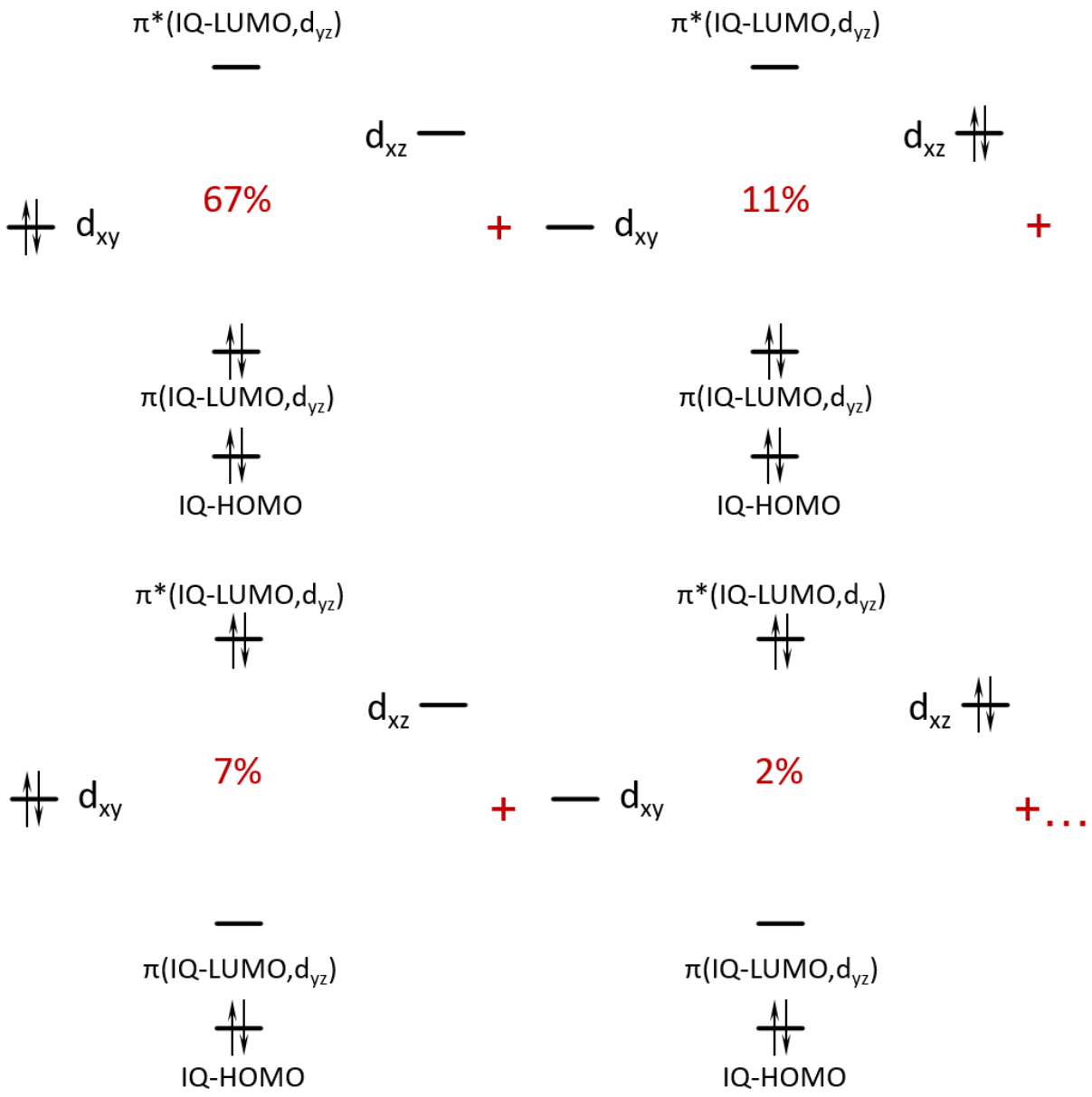

Fig. S15. Occupations of the MOs in the configurations contributing mainly to the wave function of the lowest excited singlet state of complex **2m**.

The first excited singlet state of complex **2m**, like **1m**, has a strongly multi-configuration wave function with major contributions of four electronic configurations with doubly occupied d_{xy} or d_{xz} orbitals and redistribution of electrons between π- and π*-orbitals (Fig. S14). The wave function of the first excited quintet state has a single dominant configuration (94 %) with singly occupied d_{xy}, d_{xz}, π- and π*-MOs. The Mulliken spin population on the Re ion in the quintet state is 2.73 at CASSCF level, while that of the iminooxolene ligand is 1.08.

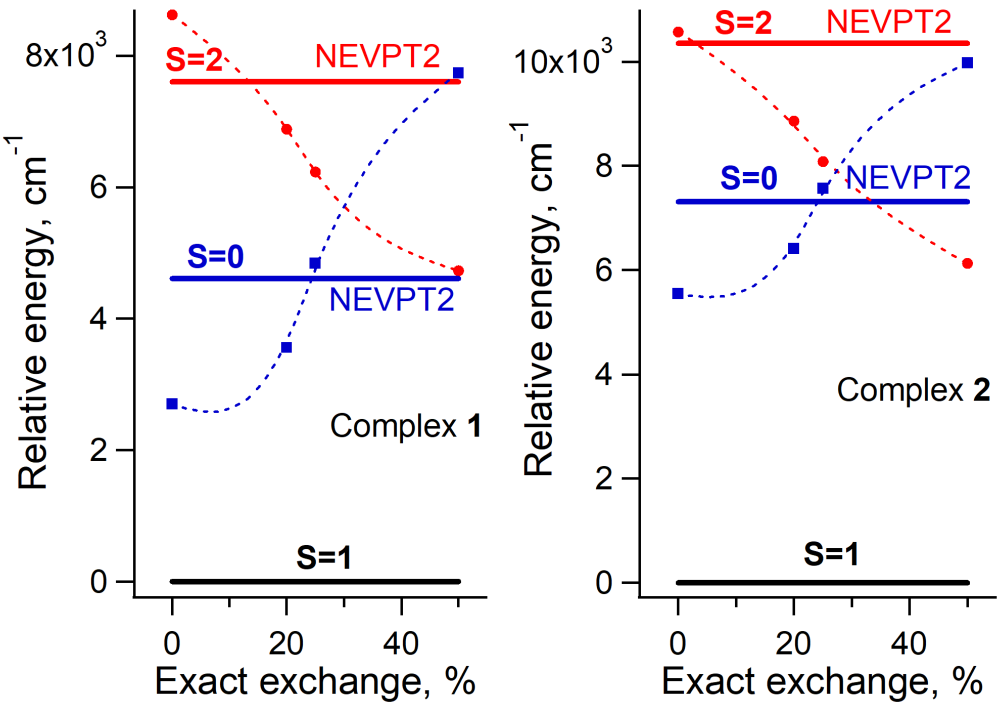

Fig. S16. The energies of the lowest singlet (blue squares) and quintet (red circles) states relative to the lowest triplet state of complexes **1m** (left) and **2m** (right) calculated at DFT level. The X-axis corresponds to the contribution of HF exchange (0 – BP86, 0.2 – B3LYP, 0.25 – PBE0, 0.5 – BHandHLYP.

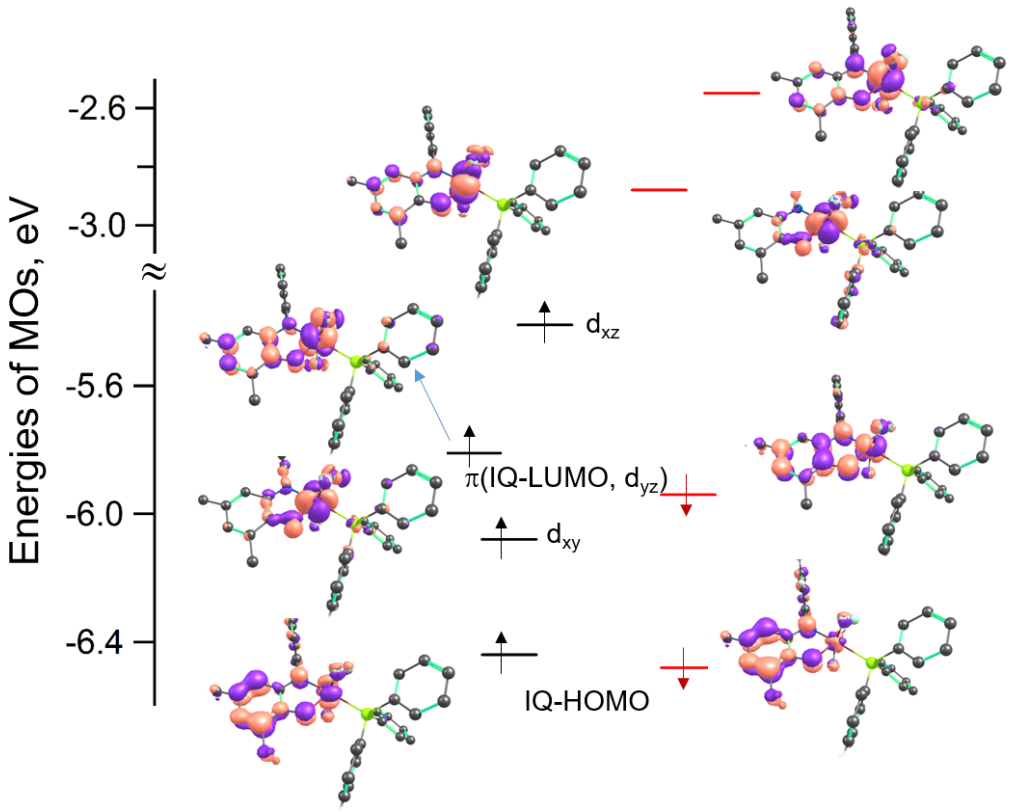

Fig. S17. The highest occupied α-MOs (isosurface at 0.052) and their β-counterparts, as well as their energies, calculated at the DKH2-UB3LYP/DKH-def2-TZVP (SARS-DKH-TAVP for Re) level for complex **1m** (hydrogen atoms have been omitted for clarity).

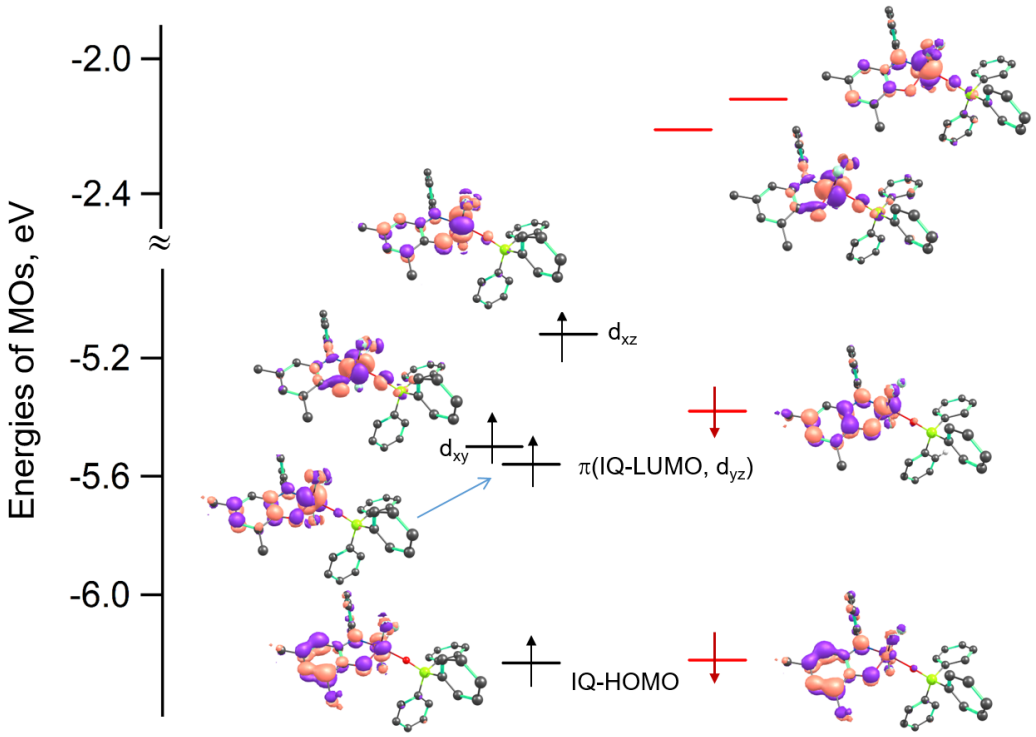

Fig. S18. The highest occupied α-MOs (isosurface at 0.052) and their β-counterparts, as well as their energies, calculated at the DKH2-UB3LYP/DKH-def2-TZVP (SARS-DKH-TAVP for Re) level for complex **2m** (hydrogen atoms have been omitted for clarity).

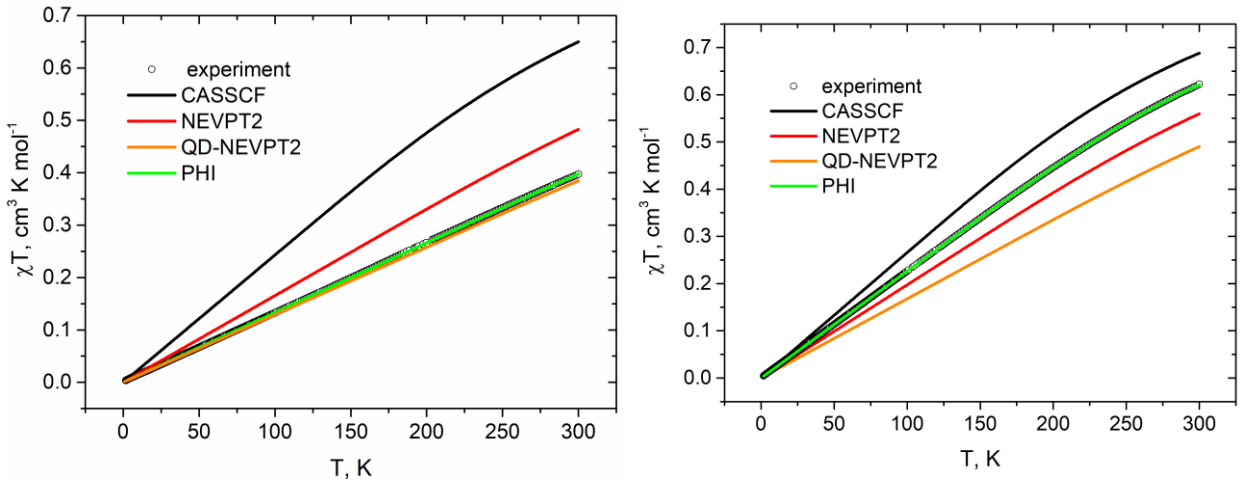

Fig. S19. Experimental temperature dependences of the product χT for complexes **1** (left) and **2** (right) obtained at a magnetic field of H = 1 kOe (black circles). Theoretical χT vs T dependences calculated using the results of SA-CASSCF(10,13)/SOC-QDPT/DKH-def2-TZVP (black curves), SA-CASSCF(10,13)/NEVPT2/SOC-QDPT/DKH-def2-TZVP (red curves) and SA-CASSCF(10,13)/QD-NEVPT2/SOC-QDPT/DKH-def2-TZVP (orange curves) calculations taking into account 1 quintets, 9 triplets and 8 singlets for both complexes. Green curves show the best fits obtained using the spin-Hamiltonian and PHI program as described in the text.

In the case of **1**, the best agreement between experimental and theoretical χT vs T dependences was achieved using the QD-NEVPT2 approach, whereas in the case of **2**, it overestimated the D value and NEVPT2 gives a closer result. The admixture of the exited singlet states to the ground triplet state was found to be essential to reproduce the splitting of the latter (Tables S2, S3; Figure S19). These singlet states have an electronic configuration similar to that of the ground triplet state. Their contribution rises from CASSCF to QD-NEVPT2 levels from 4.4% to 10.5% for **1** and from 3% to 8.5% for **2**.

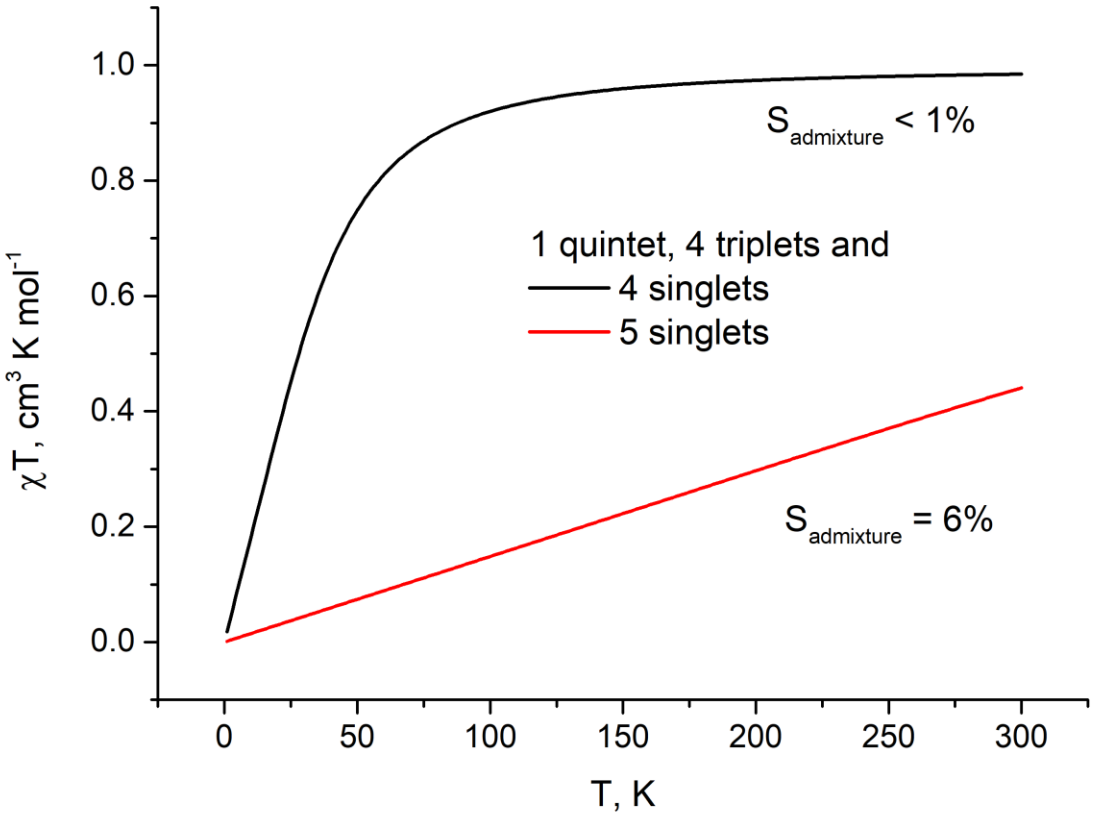

Fig. S20. Theoretical temperature dependences of the χT product for the **2m** complex calculated at the DKH2-SA-CASSCF(10,13)/QD-NEVPT2/SOC-QDPT)/DKH2-def2-TZVP level considering 1 quintet, 4 triplet, and different number of singlet states: 4 (black curve) and 5 (red curve).

Figure S19 shows that the theoretical temperature dependence of the χT product dramatically affected by the inclusion of the 5th singlet state in the SA-CASSCF calculations. This state resembles the ground triplet state and the 1st excited singlet state in terms of the occupation of active MOs. It is these singlet states that are strongly mixed into the lower sublevel of the ground triplet state when SOC is taken into account, which in turn leads to a sharp change in the behavior of χT.

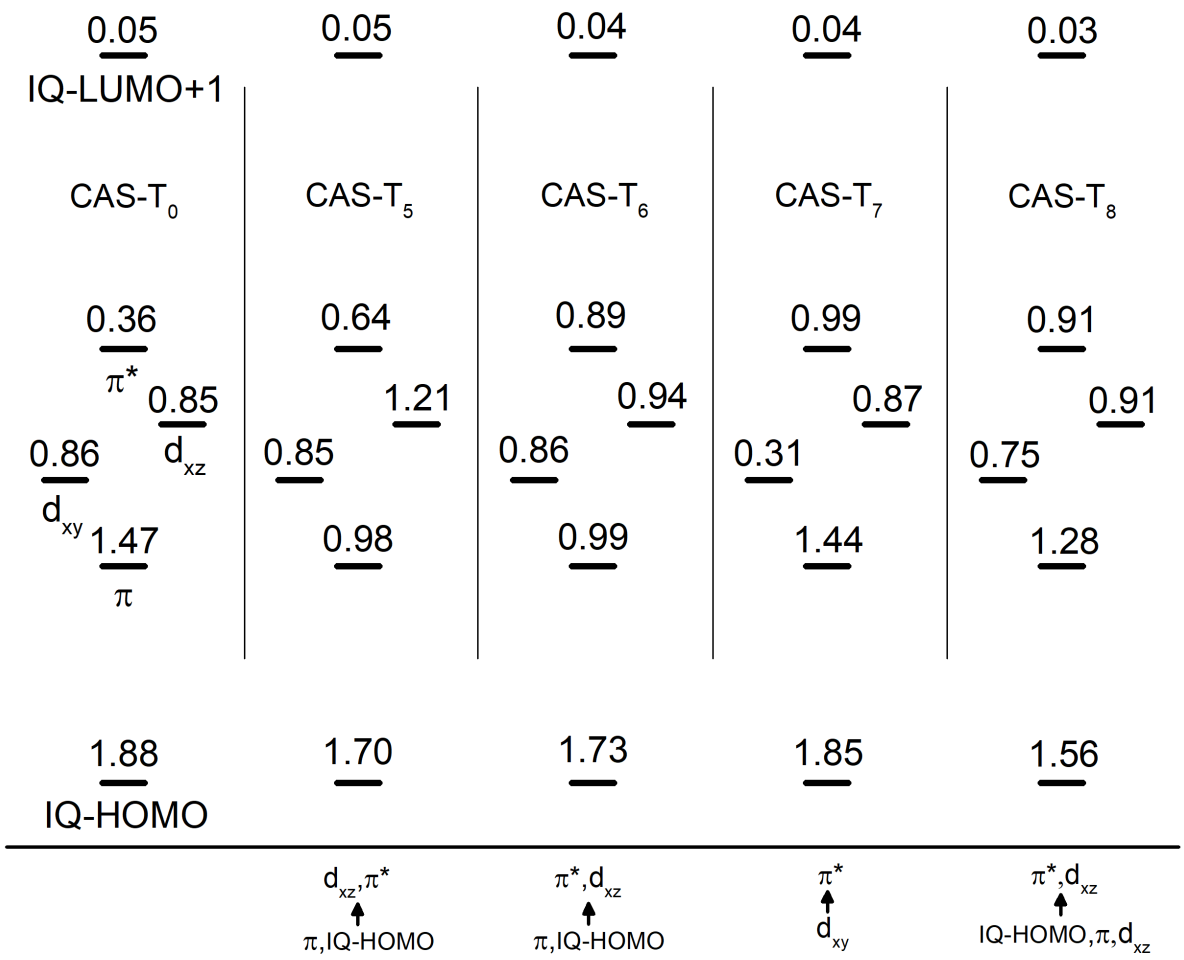

Fig. S21. Occupation numbers of active MOs in the ground and excited triplet states calculated for the **1m** complex at the SA-CASSCF(10,13)/QD-NEVPT2/ DKH2-def2-TZVP level.

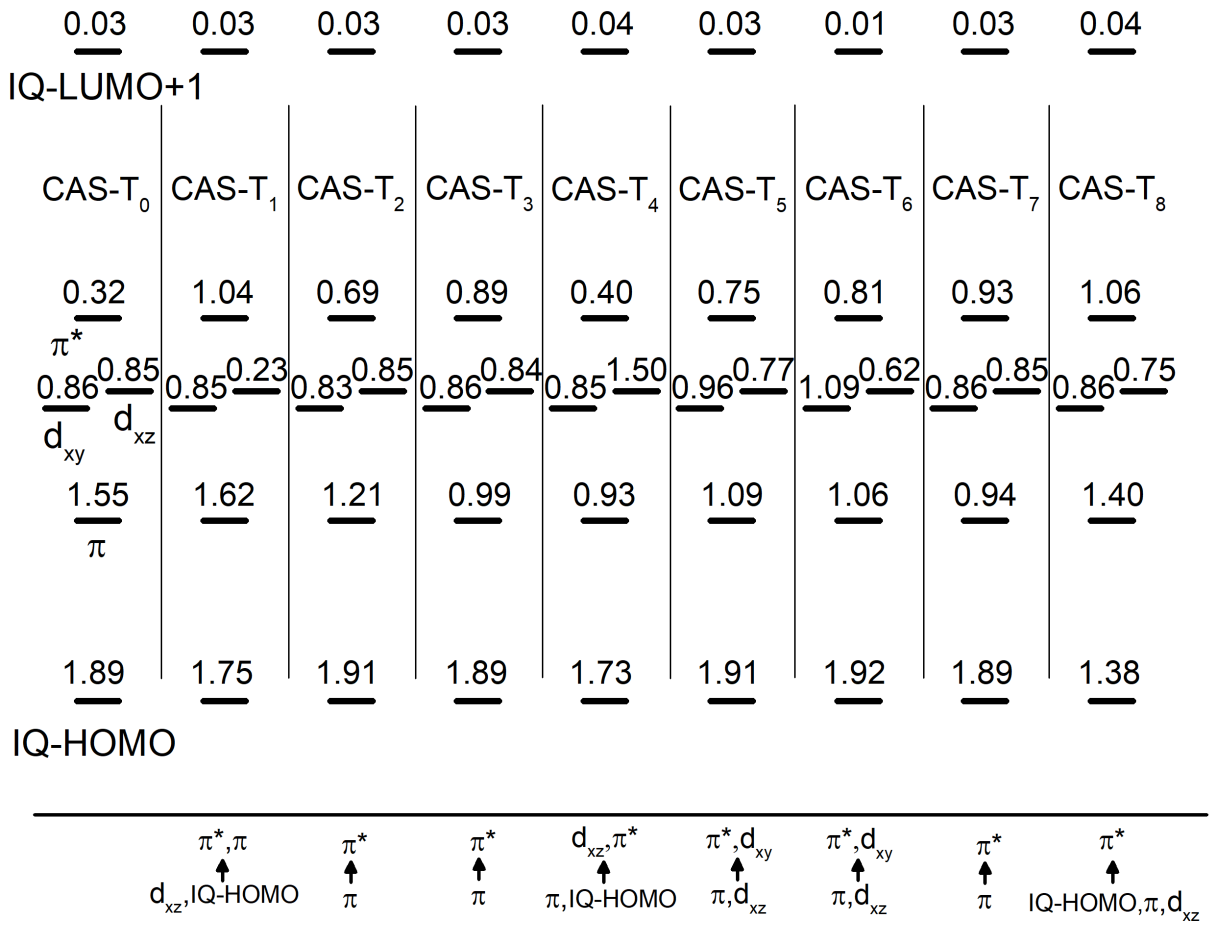

Fig. S22. Occupation numbers of active MOs in the ground and excited triplet states calculated for the **2m** complex at the SA-CASSCF(10,13)/QD-NEVPT2/def2-TZVP-DKH2 level.

Table S2. Compositions of wave functions with certain S and M_S from the CASSCF calculations, corresponding to three sublevels of the **1m** complex, arising from the ground triplet multiplet due to the SOC.

Sub-state	NEVPT2					QD-NEVPT2				
	E, cm^{-1}	Weight	Root	Spin	Ms	E, cm^{-1}	Weight	Root	Spin	Ms
0	0	0.440	0	1	1	0	0.431	0	1	1
		0.0197	0	1	0		0.018	0	1	0
		0.434	0	1	-1		0.431	0	1	-1
		0.058	0	0	0		0.079	0	0	0
		0.030	5	0	0		0.026	5	0	0
1	737	0.068	1	1	1	950	0.080	0	1	1
		0.845	1	1	0		0.821	0	1	0
		0.068	1	1	-1		0.080	0	1	-1
		0.013	6	0	0					
2	776	0.433	1	1	1	971	0.420	0	1	1
		0.114	1	1	0		0.140	0	1	0
		0.433	1	1	-1		0.420	0	1	-1

Table S3. Compositions of wave functions with certain S and M_S from the CASSCF calculations, corresponding to three sublevels of the **2m** complex, arising from the ground triplet multiplet due to the SOC.

State	NEVPT2					QD-NEVPT2				
	E, cm^{-1}	Weight	Root	Spin	Ms	E, cm^{-1}	Weight	Root	Spin	Ms
0	0	0.065492	0	1	1	0	0.065818	0	1	1
		0.802334	0	1	0		0.796432	0	1	0
		0.065492	0	1	-1		0.065818	0	1	-1
		0.046665	5	0	0		0.014271	0	0	0
							0.043899	5	0	0
1	636	0.489164	0	1	1	762	0.489405	0	1	1
		0.489164	0	1	-1		0.489405	0	1	-1
		0.013946	6	0	0					
2	685	0.421974	0	1	1	787	0.421691	0	1	1
		0.137364	0	1	0		0.137154	0	1	0
		0.421974	0	1	-1		0.421691	0	1	-1
		0.010095	7	0	0					

The largest positive contributions to the D value come from the interactions of the ground triplet state with the first and sixth excited singlet states (427 and 535 cm^{-1}, respectively) for **1m** and with the sixth singlet state (730 cm^{-1}) for **2m**. All of these excited states have a multi-configuration composition similar to the ground triplet state, the main difference being only the occupancy of one of the d_{xy} or d_{xz} orbitals by two electrons. A rough estimate of the D values for

the lowest excited quintet states gives values close to ~140 cm^{-1} and ~60 cm^{-1} for **1m** and **2m,** which is significantly smaller than for the ground triplet states but typical for rhenium complexes.

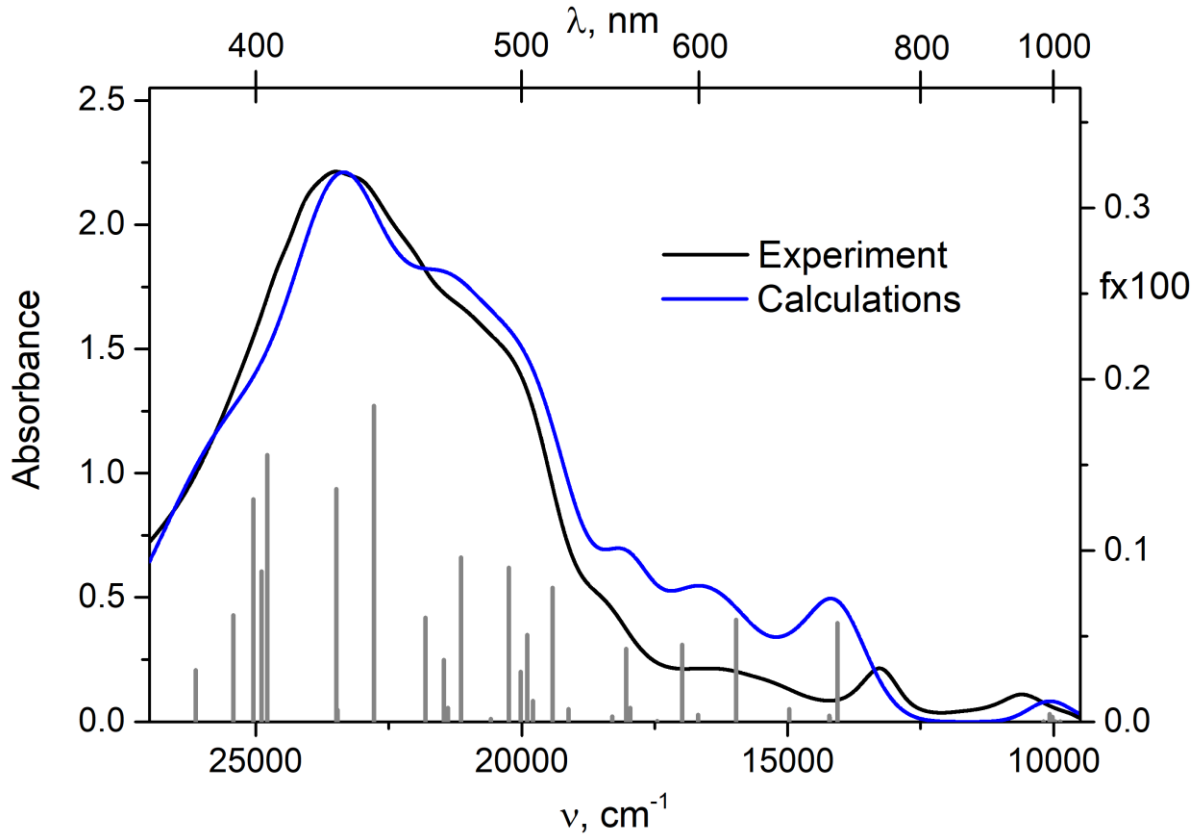

Fig. S23. Experimental electronic absorption spectrum of complex **2** in CH_2Cl_2 solution (black curve). Gray bars represent positions and oscillator strengths of electronic transitions calculated at the SA-CASSCF(10,13)/QD-NEVPT2/SOC-QDPT level taking into account 1 quintet, 9 triplets and 8 singlets for the modified complex **2m**. Blue curve corresponds to the calculated absorption spectrum assuming a Gaussian shape of the bands of individual electronic transitions using the given calculated data and the ORCA_ASA program. The bandwidths were individually chosen for each transition.

Overall, Figure S23 demonstrates very good agreement between theory and experiment. Moreover, it shows that the calculated transitions are densely distributed within the experimental spectral region (370 – 1100 nm or (27 – 9)×10^3 cm^{-1}). The most intense electronic transition is predicted to be at 439 nm (22780 cm^{-1}), which is in good agreement with the maximum at 426 nm (23470 cm^{-1}) and corresponds to excitation from the ground state to the 32th magnetic sublevel. This sublevel has a larger contribution from the 5th (T_5, 33%) and 6th (T_6, 19%) triplet and 6th (23%) singlet states. Figure S22 shows that the T_0 → T_5 and T_0 → T_6 transitions lead to the population of π* and d_{xy} MOs at the expense of π and d_{xz}. Considering the composition of π and π*, it can be concluded that the transition under consideration is a superposition of LMCT, intra-ligand and d-d transitions.

The shoulder around 490 nm (~20410) can be attributed to two strong calculated transitions at 473 and 494 nm, corresponding to excitations to the 28th and 26th magnetic sublevels. A closer

look reveals similarities in the nature of these transitions. The 28th sublevel is a superposition of the 6th (28%), 4th (22%), 8th (16%), and 5th (12%) triplet states, while the 26th sublevel has two largest contributions from the 4th (50%) and 6th (22%) triplet states. According to the Figure S22, the $T_0 \rightarrow T_4$ transition is mainly the π-to-d_{xz} electron transition, while $T_0 \rightarrow T_8$ is determined by the IQ-HOMO depopulation in favor of π*. Thus, like the previous transition, it has a complex nature.

As in the case of complex **1**, the long-wavelength band at 943 nm (10600 cm^{-1}) is related to spin-forbidden transitions. Two close in position (998 and 992 nm) and in intensity calculated transitions correspond to the excitations to the 7th and 8th sublevels. Both sublevels originate from the 0th quintet and 1st singlet states, namely, the 7th is a superposition of 71% quintet and 26% singlet, and the 8th is 81% quintet and 14% singlet.

The next three experimental absorption bands are characterized by maxima at about 753 and 608 (13280 and 16450 cm^{-1}) and shoulder at 545 nm (18359) and can be roughly attributed to the transitions from the ground to the 1st, 2nd and 3rd triplets. More specifically, the calculated intense transition at 711 nm (14060 cm^{-1}) corresponds to the excitation to the 10th sublevel, which is 78% of the 1st triplet. The $T_0 \rightarrow T_1$ is mainly a d_{xz} to π* transition, namely a combination of d-d and MLCT. The next two calculated transitions at 626 and 589 nm (15970 and 16980 cm^{-1}) originate from the excitations to the 14th and 16th sublevels. The 14th sublevel has 38% of 2nd triplet and 29% of 3rd singlet states, while the 16th sublevel consists of the 2nd triplet (44%) and 3rd singlet (36%) states. The last transition at 555 nm (18020 cm-1) occurs to the 19th sublevel with 57% of the 3rd and 13 % of the 2nd triplet states. Both $T_0 \rightarrow T_2$ and $T_0 \rightarrow T_3$ lead to a population transfer from π to π*, i.e. they partially have a LMCT character.

IV. Cyclic Voltammetry Data and Crystal Structure of Complex 3

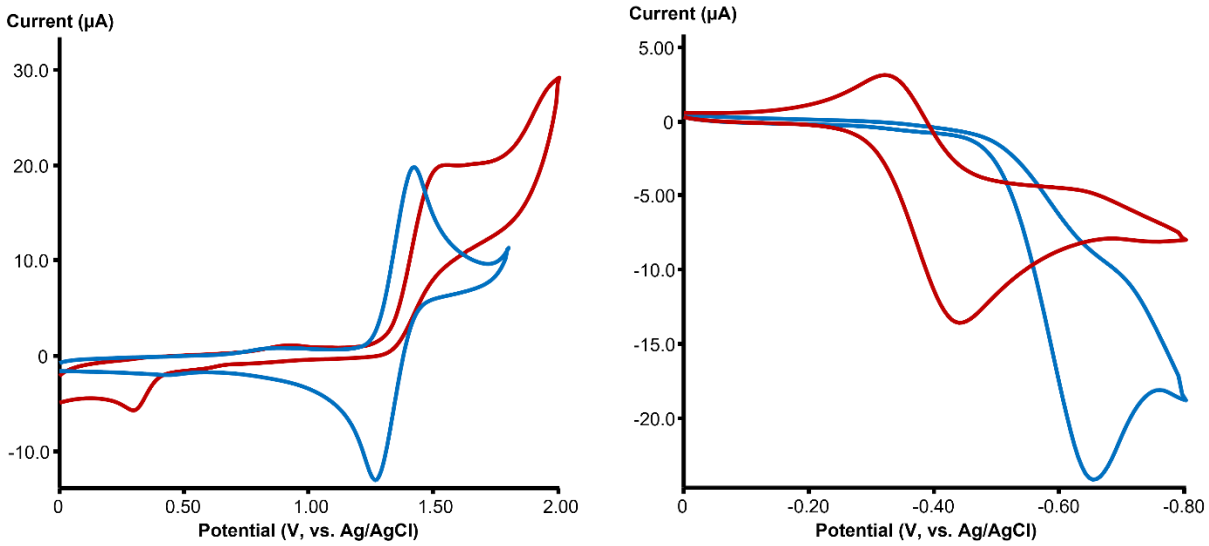

Fig. S24. Cyclic voltammograms of complexes **1** (red line) and **2** (blue line) in CH_2Cl_2 at a potential scan rate of 100 mV/s: left – oxidation; right – reduction.

Complexes **1** and **2** differ significantly in their electrochemical stability: complex **1** is irreversibly oxidized at E_p^{ox} = 1.50 V, while complex **2** exhibits reversible oxidation at $E_{1/2}$ = 1.35 V. On the other hand, complex **2** is irreversibly reduced at E_p^{red} = –0.64 V. Complex **1** is more readily reduced, its reduction potential is noticeably shifted toward a more anodic region ($E_{1/2}$ = –0.38 V), and its reduction is more reversible. However, the current ratio I_a/I_c deviates significantly from unity, indicating that this process is not completely reversible. Thus, a reversible or quasi-reversible process is observed for only one of the complexes (for **2** during oxidation and for **1** during reduction). Therefore, only E_p^{red} (the reduction peaks) or E_p^{ox} (the oxidation peaks) can be compared for **1** and **2**. It can be seen from the Figure that the difference in potentials of the oxidation peaks ($E_p^{ox}(1) - E_p^{ox}(2)$) is noticeably less (113 mV) than the difference in reduction peaks ($E_p^{red}(1) - E_p^{red}(2)$=220 mV).

In the calculations, the half-wave potentials ($E_{1/2}$) are determined. It is reasonable to assume that the difference in reduction or oxidation potentials is close to the difference of corresponding half-wave potentials. The potential of the first half-wave can be calculated using the free energy of reduction ($A + e \rightarrow A^-$) or oxidation ($D^+ + e \rightarrow D$) reactions (ΔG_r) according to the formula

$$E_{1/2}^{red,ox} = constant(electrode, solvent) - \Delta G_r/F,$$

where the constant depends only on the electrode type and solvent.

For complexes **1** and **2**, geometry optimization was performed using the (U)B3LYP functional with the def2-TZVP basis set (with ECP for Re), the RIJCOSX approximation with the def2/J auxiliary basis set and DefGrid3. Recall that for both complexes the ground state is triplet, so oxidation / reduction can produce ions with multiplicity 2 or 4. Multiplicities 4 and 2 were used for the anionic and cationic forms of complexes, respectively, since for both

complexes, it was found that anions with a multiplicity 4 have lower energies than anions with a multiplicity of 2 and vice versa for cations.

The difference of the calculated half-wave potentials of reduction ($E_{1/2}^{red}(1) - E_{1/2}^{red}(2)$) is 340 mV, which is in good agreement with the experiment difference in the potentials of reduction peaks (220 mV). In the case of oxidation, the calculated difference of the half-wave potentials ($E_{1/2}^{ox}(1) - E_{1/2}^{ox}(2)$) is 110 mV, which is almost identical to the experimental difference in the oxidation peak potentials (113 mV).

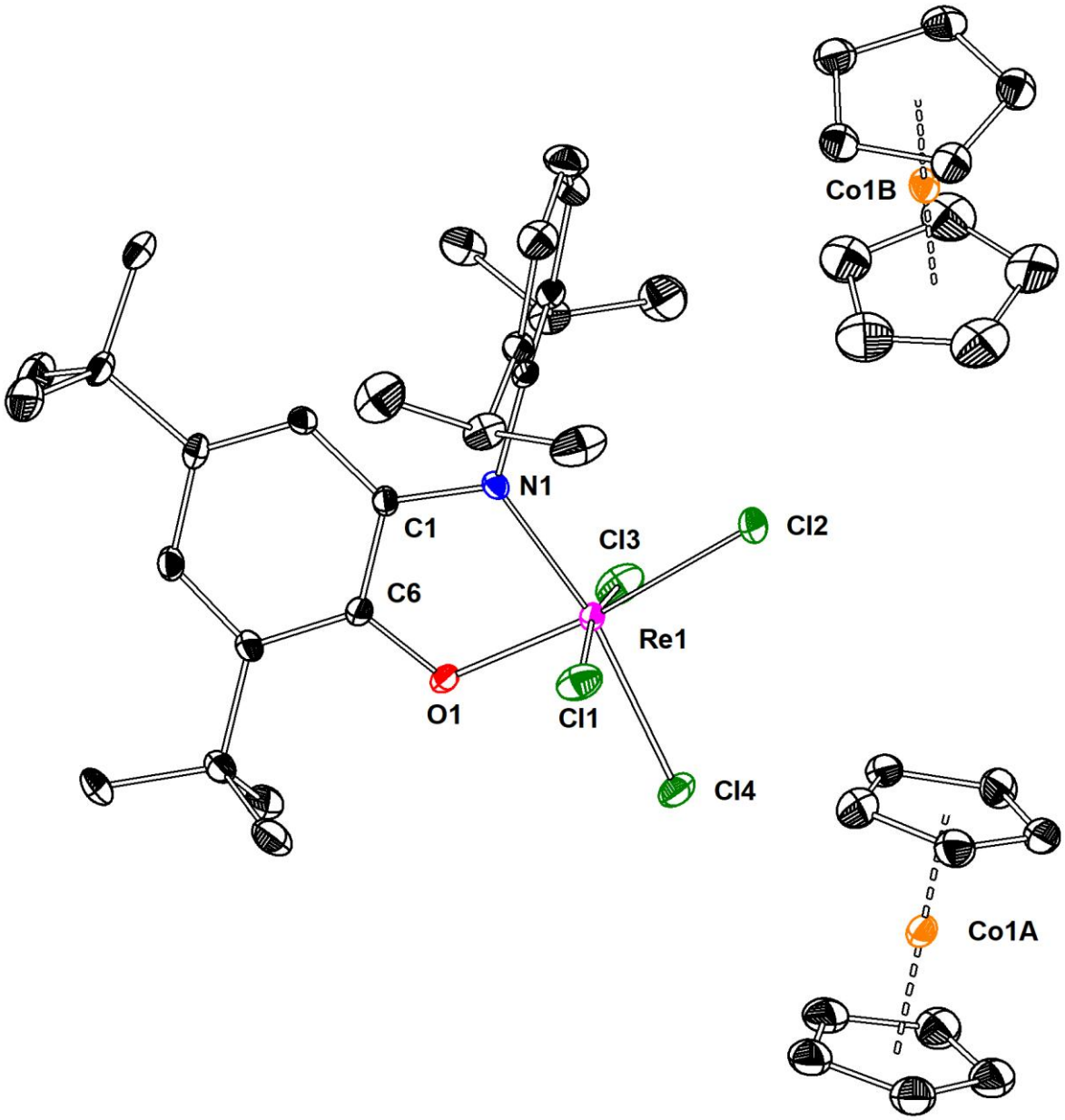

Fig. S25. Molecular structures of complex **3**. Thermal ellipsoids are given in 30% probability. Hydrogen atoms are omitted for clarity. Selected bond lengths (Å): Re1–Cl1 2.3696(17), Re1–Cl2 2.3211(16), Re1–Cl3 2.3397(18), Re1–Cl4 2.3841(16), Re1–O1 1.980(4), Re1–N1 2.003(5), O1–C6 1.329(8), N1–C1 1.372(8), C1–C6 1.414(9).

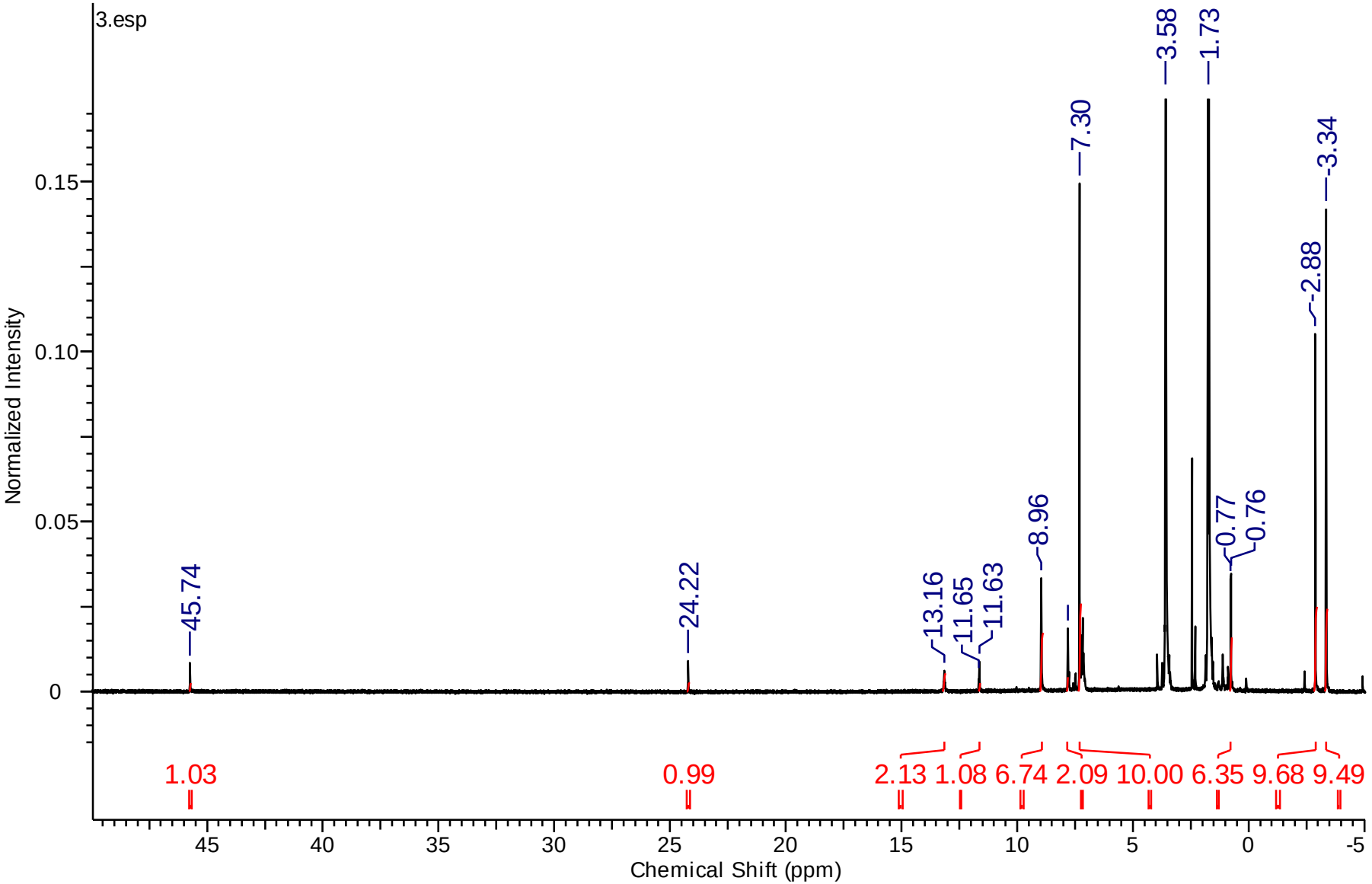

Fig. S26. ^{1}H NMR spectrum of complex **3** (thf-d_8, ambient temperature).

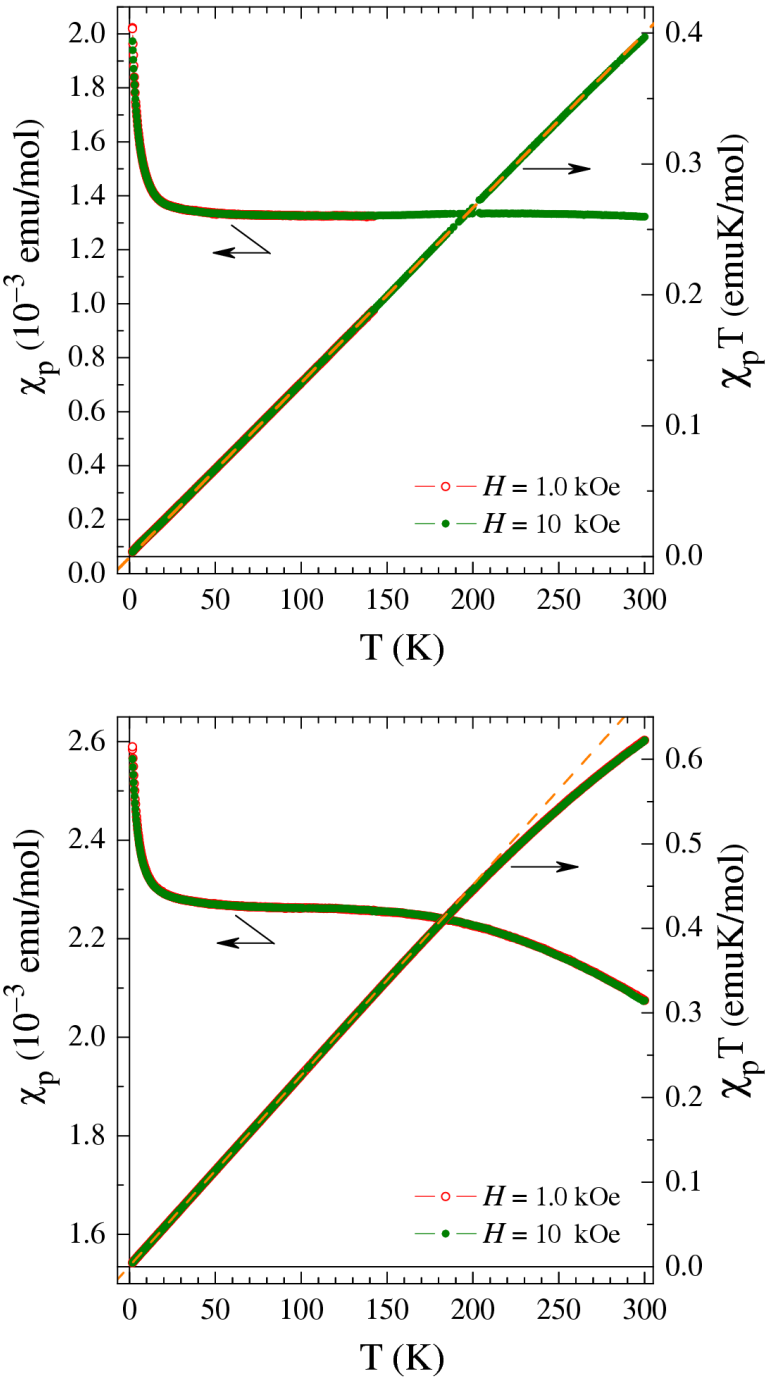

Fig. S27. Temperature dependences of the paramagnetic component of the magnetic susceptibility χ_p and the product χ_pT, measured for **1** (top) and **2** (bottom) at magnetic fields H = 1, 10 kOe.

Table S4. Calculated MOS values for known Re complexes with iminoxolene ligands

Refcode	Formula	MOS	Reference
CAWMOD	$[Re^{II}(CO)_2(ISQ^{Dipp})_2]$	–1.15(9), –1.16(8)	S1
LUSKIU	$[Re^{V}O(AP^{Ph})_2]^-$	–2.13(6), –2.09(7)	S2
LUSKOA	$[Re^{VII}O_2(AP^{Ph})_2]^-$	–1.82(12), –1.81(9)	S2
IBUNAW	$[Re^{VI}O(AP^{Ph})(ISQ^{Ph})Cl]$	–1.96(8), –0.93(7)	S3
IBUMUP	$[Re^{VI}O(AP^{Ph})(ISQ^{Ph})(OC_6Cl_5)]$	–1.87(12), –0.98(11)	S3
IBUNIE	$[Re(L^{Ph})_2Cl_2]$	–1.25(9), –1.22(8)	S3

References

S1. Abakumov, G. A., Poddel'sky, A. I., Bubnov, M. P., Fukin, G. K., Abakumova, L. G., Ikorskii, V. N., Cherkasov, V. K. Manganese(III) and rhenium(II) complexes with bulky 4,6-di-tert-butyl-N-(2,6-di-iso-propylphenyl)-o-iminobenzoquinonato ligands via carbonyls of corresponding metals. *Inorg. Chim. Acta*, **2005**, *358*, 3829–3840.

S2. Lippert, C.A., Arnstein, S.A., Sherrill, C.D., Soper, J.D. Redox-active ligands facilitate bimetallic O_2 homolysis at five-coordinate oxorhenium(V) centers. *J. Am. Chem. Soc.*, **2010**, *132*, 3879–3892.

S3. Lippert, C.A., Hardcastle, K.I., Soper, J.D. Harnessing redox-active ligands for low-barrier radical addition at oxorhenium complexes. *Inorg. Chem.*, **2011**, *50*, 9864–9878.